



Article

Enhancing Performance of Millimeter Wave MIMO Antenna with a Decoupling and Common Defected Ground Approach

Poonam Tiwari ¹, Vishant Gahlaut ¹, Meenu Kaushik ², Anshuman Shastri ³ , Vivek Arya ^{4,*}, Issa Elfergani ^{5,6,*} , Chemseddine Zebiri ⁷ and Jonathan Rodriguez ⁵

¹ Department of Physical Sciences, Banasthali Vidyapith, Banasthali 304022, RJ, India; tpoonam@banasthali.ac.in (P.T.); gvishant@banasthali.in (V.G.)

² School of Automation, Banasthali Vidyapith, Banasthali 304022, RJ, India

³ Centre for Artificial Intelligence, Banasthali Vidyapith, Banasthali 304022, RJ, India; anshumanshastri@banasthali.in

⁴ Department of Electronics and Communication Engineering, Faculty of Engineering and Technology, Gurukula Kangri (Deemed to be University) Haridwar 249404, UK, India

⁵ Instituto de Telecomunicações, Campus Universitário de Santiago, 3810-193 Aveiro, Portugal; jonathan@av.it.pt

⁶ School of Engineering and Informatics, University of Bradford, Bradford BD7 1DP, UK

⁷ Laboratoire d'Electronique de Puissance et Commande Industrielle (LEPCI), Department of Electronics, University of Ferhat Abbas, Sétif -1-, Sétif 19000, Algeria; czebiri@univ-setif.dz

* Correspondence: vivek.arya@gkv.ac.in (V.A.); i.t.e.elfergani@av.it.pt or i.elfergani@bradford.ac.uk (I.E.)

Abstract: An approach is presented to enhance the isolation of a two-port Multiple Input Multiple Output (MIMO) antenna using a decoupling structure and a common defected ground structure (DGS) that physically separates the antennas from each other. The antenna operates in the 24 to 40 GHz frequency range. The innovation in the presented MIMO antenna design involves the novel integration of two arc-shaped symmetrical elements with dimensions of $35 \times 35 \times 1.6 \text{ mm}^3$ placed perpendicular to each other. The benefits of employing an antenna with elements arranged perpendicularly are exemplified by the enhancement of its overall performance metrics. These elements incorporate a microstrip feed featuring a quarter-wave transformer (QWT). This concept synergizes with decoupling techniques and a defected ground structure to significantly enhance isolation in a millimeter wave (mm wave) MIMO antenna. These methods collectively achieve an impressively wide bandwidth. Efficient decoupling methodologies have been implemented, yielding a notable increase of 5 dB in isolation performance. The antenna exhibits 10 dB impedance matching, with a 15 GHz (46.87%) wide bandwidth, excellent isolation of more than 28 dB, and a desirable gain of 4.6 dB. Antennas have been analyzed to improve their performance in mm wave applications by evaluating diversity parameters such as envelope correlation coefficient (ECC) and diversity gain (DG), with achieved values of 0.0016 and 9.992 dB, respectively. The simulation is conducted using CST software. To validate the findings, experimental investigations have been conducted, affirming the accuracy of the simulations.

Keywords: DGS; decoupling structure; mm wave; MIMO; 5G; QWT



Citation: Tiwari, P.; Gahlaut, V.; Kaushik, M.; Shastri, A.; Arya, V.; Elfergani, I.; Zebiri, C.; Rodriguez, J. Enhancing Performance of Millimeter Wave MIMO Antenna with a Decoupling and Common Defected Ground Approach. *Technologies* **2023**, *11*, 142. <https://doi.org/10.3390/technologies11050142>

Academic Editors: Johan Jair Estrada-López, Alejandro A. Castillo Atoche and Javier Vázquez-Castillo

Received: 25 September 2023

Revised: 8 October 2023

Accepted: 10 October 2023

Published: 16 October 2023



Copyright: © 2023 by the authors. Licensee MDPI, Basel, Switzerland. This article is an open access article distributed under the terms and conditions of the Creative Commons Attribution (CC BY) license (<https://creativecommons.org/licenses/by/4.0/>).

1. Introduction

In a world driven by the growing need for high-speed wireless communications, researchers and innovators are working hard to advance fifth generation (5G) wireless networks [1]. The demand for fast data transmission has increased, especially with the rise of the Internet of Things (IoT), smart homes, industrial automation, and remote medical services [2]. The challenge lies in overcoming the congestion that plagues existing systems, which is where 5G comes in [3–5]. Utilizing this means venturing into the higher-frequency bands that are capable of supporting these increased data speeds [6]. However, as with any progress, there are obstacles that have to be overcome. Employing shorter wavelengths

in the higher-frequency band has a drawback: increased path loss for short-distance communications [7,8]. This implies that signals become weaker and attenuate faster, resulting in reduced coverage [9]. This is a challenge that must be addressed for 5G to reach its full potential. Despite these obstacles, researchers are determined to find the right solution [10]. Various types of antennas have been examined for their suitability in 5G communication bands. These include the short dipole antenna [11], microstrip patch antenna [12], ultra-wideband horn antenna [13], loop antenna [14], slot antenna [15], aperture antenna [16], Yagi–Uda antenna [17], leaky-wave antenna [18], and log-periodic antenna [19]. Different types of antennas have been put under the microscope for their suitability in the 5G communication bands [20]. These antennas have gained popularity in wireless communication due to their advantageous features. With their low profile, compact size, and cost-effective manufacturing, microstrip antennas are well-suited for 5G technology applications [21,22].

Innovative techniques such as implementing a decoupler and common DGS show promise. The decoupler effectively minimizes mutual coupling between antenna elements, while the DGS structure suppresses surface wave propagation along the ground plane, reducing interference and improving overall antenna performance [23]. As the world continues towards an ever-expanding realm of wireless communication, researchers are continuously exploring methods by which to tackle the challenges posed by mm wave MIMO antennas [24]. From neutralization lines to electromagnetic band gap structures, diversity techniques, and decoupling structures, each approach seeks to enhance isolation performance at specific frequency bands commonly used in 5G wireless systems [25]. One fundamental approach involves manipulating the physical arrangement of the antenna elements. Techniques such as element spacing, orientation, and polarization are explored to reduce the coupling effect [26]. Innovative electromagnetic structures, such as metamaterials and electromagnetic band gap (EBG) structures, are employed to control the coupling between antenna elements [27].

Yet challenges persist, especially in terms of integrating multiple antennas into compact portable devices. The potential coupling issues can severely impact the diversity performance of antennas [28]. Metamaterial-inspired structures, such as capacitive-loaded loops [29], split-ring resonators [30], and metamaterial superstrates [31], have proven effective at enhancing the isolation of MIMO antennas. However, integrating these structures can lead to challenges such as increased space requirements and heightened design intricacies [32]. This complexity arises from the integration of intricate RF circuits into compact communication devices. Consequently, contemporary research is actively focused on elevating the performance of printed MIMO technology. This emphasis is placed on optimizing antenna gain, bandwidth, isolation, and radiation properties while minimizing both design complexity and associated costs. Ensuring high isolation has become a crucial task for optimal functionality in MIMO communication systems, particularly in the world of portable devices [33]. Many decoupling techniques involve trade-offs between antenna performance metrics, such as isolation, gain, and bandwidth. Achieving one objective might negatively impact others. Moreover, some advanced techniques increase the complexity of the system, requiring careful consideration of the associated costs and benefits [34]. MIMO systems often operate in multiple frequency bands, which makes it challenging to apply a single decoupling technique across all bands. Solutions that work well in one band might not perform optimally in another. The practical implementation of certain decoupling techniques can be complex and may pose challenges during the manufacturing process or integration into compact devices [35].

Environmental effects and Real-World Conditions: The performance of decoupling techniques can vary under different environmental conditions, such as varying electromagnetic environments and interference sources. Accurately testing and validating the effectiveness of decoupling techniques in real-world scenarios can be difficult, and may require sophisticated measurement setups and simulations [36].

In this study, a two-port arc-shaped MIMO antenna with a common DGS incorporates a compact and highly integrated decoupling structure. The unique arc shape is chosen for its ability to create an extended electrical path within a limited space, resulting in a compact, yet efficient, antenna design. The MIMO configuration employs an orthogonal arrangement of antennas to minimize undesired interaction between elements. The DGS operates at the intersection of electromagnetic wave behavior and material characteristics. Using dielectric guides improves the paths of coupling currents for higher efficiency while reducing mutual coupling by changing how fields interact. This approach leverages fundamental electromagnetic principles to improve isolation and overall antenna performance. To further enhance isolation, the proposed decoupling structure effectively addresses the gap between antennas, thereby boosting system performance and efficiency. The MIMO structure positions antennas orthogonally to mitigate undesirable electromagnetic coupling. Nevertheless, the achieved performance fell within the desired range for MIMO applications in different countries such as those in Europe (26.5–27.5 GHz), as well as China (24.25–27.5 GHz), Japan (28.2–29.1 GHz, 29.1–29.5 GHz, 39.5–40 GHz), Republic of Korea (26.5–29.5 GHz), the USA (24.25–29.5 GHz and 37–40 GHz), and Sweden (26.5–27.5 GHz), covering the target frequency bands. A wideband antenna spanning the 24 to 40 GHz frequency range serves a diverse range of applications, including 5G communication, radar systems, satellite links, remote sensing, wireless backhaul, imaging, security screening, scientific research, and automotive radar. Its capability to operate across this broad frequency spectrum renders it a versatile choice for high-frequency communication and sensing tasks.

Table 1 illustrates the superiority, and Table 2 demonstrates the advantages and demerits, of the proposed compact mm wave antenna compared with previous designs. The proposed approach operates within the 25–40 GHz frequency range, measures $35 \times 35 \text{ mm}^2$ in size, has two ports, and combines decoupling and DGS techniques. It achieves exceptional isolation performance, exceeding 28.7 dB, surpassing most referenced works. The extremely low envelope correlation coefficient (ECC) of 0.0016 demonstrates improved signal isolation. Additionally, the diversity gain (DG) metric indicates signal degradation exceeds 9.992. Compared with existing references, the proposed work not only enhances isolation but also offers a wider 15 GHz bandwidth for efficient signal handling. This study presents a superior approach by which to enhance isolation and maintain signal integrity in the specified frequency range, with its compact design, improved isolation, and wider bandwidth setting it apart from previous works.

This study thoroughly examines a MIMO antenna design using CST simulations and validates the results with a physical prototype analyzed via a Rohde and Schwarz ZNB 40 vector network analyzer (VNA). Section 1 introduces the integration of mm wave into MIMO antennas, emphasizing the use of DGS and decoupling techniques. It includes a comparative analysis against existing literature (Tables 1 and 2). Section 2 covers the single antenna design evolution and performance analysis. Section 3 outlines the MIMO antenna configuration with specific dimensions in Table 3. Section 4 demonstrates the parametric analysis of the proposed antenna. Section 5 presents simulated results and discussion, while measurement analysis is presented in Section 6. Section 7 delves into diversity performance, and finally, Section 8 provides a summary and conclusion.

Table 1. Comparison of the proposed antenna design with the existing literature.

Ref.	Frequency (GHz)	Size	Number of Ports	Substrate Used	Technique	Bandwidth (GHz)	Isolation (dB)	ECC	DG (dB)
[37]	24–34	11×20.5	2	RT Duroid 5880	Defected connected ground	10	>23.6	<0.044	>9.99
[38]	24–29.9	23×24	2	RT Duroid 5880	Metamaterial	5.5	>24	<0.0013	>9.9

Table 1. Cont.

Ref.	Frequency (GHz)	Size	Number of Ports	Substrate Used	Technique	Bandwidth (GHz)	Isolation (dB)	ECC	DG (dB)
[39]	23–40	80 × 80	4	RT Duroid 5880	Simple full ground	16	>10	<0.0014	>9.6
[40]	25.5–29.6	30 × 35	4	Rogers R04350B	Defected ground	4.1	>17	<0.001	>9.99
[41]	27.5–40	18.2 × 4.1	2	RT Duroid 5880	Electromagnetic band gap (EBG)	12.5	>15	Not provided	Not provided
[42]	25.30–42	12 × 45.2	4	RT Duroid 5880	Defected ground	16.7	>24	0.0003	9.97
[43]	25.1–37.5	12 × 50.8	4	RT Duroid 5880	Defected ground	12.4	>22	0.005	9.9
[34]	27–40	55.25 × 27.635	2	FR-4	Decoupling structure	13	>30	0.00003	9.9994
[44]	26–42	26 × 11	2	RT Duroid 5880	Separate defected ground	2.5, 6	>25	0.16	9.986
Presented work	25–40	35 × 35	2	RT Duroid 5880	Decoupling and defected connected ground	15	>28.7	0.0016	>9.992

Table 2. Comparative advantages and demerits of proposed antenna with existing literature.

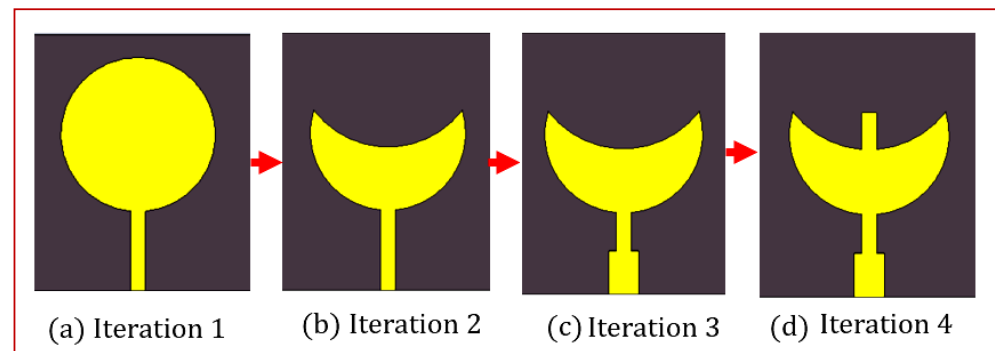
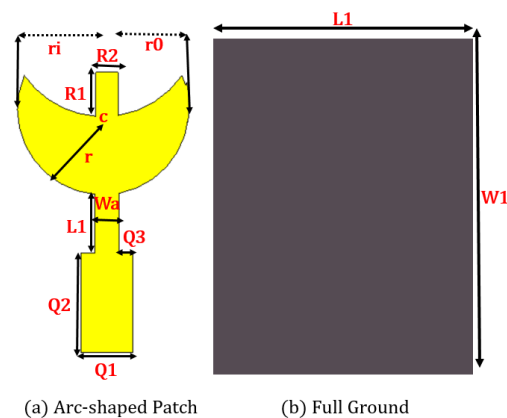
Ref.	Advantages	Demerits
[37]	Wide bandwidth (10 GHz), good isolation (>23.6 dB)	Moderate size
[38]	High isolation (>24 dB), metamateria technique	Limited bandwidth, moderate size.
[39]	Good isolation	Lower isolation and ECC
[40]	Decent isolation (>17 dB), low ECC)	Limited bandwidth, moderate size.
[41]	Small size, wide bandwidth	Limited frequency range, low isolation no ECC or DG data provided
[42]	Wide bandwidth (16.7 GHz), high isolation (>24 dB)	Moderate size, 4 ports
[43]	Good isolation and reasonable bandwidth.	Moderate size, 4 ports
[34]	Very high isolation (>30 dB), low DG	Limited bandwidth, large size.
[44]	Large size, moderate isolation	Limited bandwidth
Proposed Work	Wide bandwidth (15 GHz), high isolation (>28.7 dB), low ECC and DG	Large size

Table 3. Parametric symbols and dimensions.

Symbols	Dimensions (mm)	Symbols	Dimensions (mm)
L1	17.5	Ri	4.8
W1	17.5	Ro	4.85
L2	35	B	1.2
W2	35	A	0.8
Wa	1.65	M	2.83
Q1	3.25	N	13.33
Q2	6.75	G0=G5=G9=G13	1.27
Q3	0.8	G1=G4=G7=G11	1.8
L1	4.80	T	1.5
R1	3.3	D _(Diameter-inner circle)	2
R2	1.8	H _(Diameter-Outer circle)	4.5
r	5.2	G3=G8=G12=G15	11.13
		G2=G6=G10=G14	12.14

2. Design Evolution of Single Antenna Configuration

The design of a high-frequency arc-shaped patch antenna consists of a copper microstrip patch printed on an RT-5880 substrate, as depicted in Figure 1d. The parameterized top and bottom views are depicted in Figure 2. The arc-shaped microstrip patch has a breadth of 0.01 mm. The 1.6 mm-thick substrate, with a dielectric constant (ϵ_r) of 2.2 and a loss tangent (\tan) of 0.009, serves as the supporting material for the antenna. The antenna has been designed to function in the 24 GHz to 40 GHz frequency range. The dimension of the single antenna is $17.5 \times 17.5 \text{ mm}^2$, with a full ground layer added at the base of the substrate. The patches are fed with 50Ω microstrip transmission lines. Additionally, for the purpose of impedance matching, a QWT is also used.

**Figure 1.** Iterative design configuration of single antenna s.**Figure 2.** Parametrized single antenna design configuration.

The initial single antenna underwent a series of four iterative optimization stages to achieve the desired performance outcomes, as depicted in Figure 1a–d. In iteration 1, the antenna is designed with a circular patch featuring a microstrip feed located on a dielectric substrate (see Figure 1a). As a result of this configuration, the antenna demonstrated a reflection coefficient ($|S_{11}|$) below -10 dB across a frequency range of 24 to 25.6 GHz (fractional bandwidth (FBW) of 5%) and 29.6 to 33.2 GHz (FBW of 11.25%), as demonstrated in Figure 3 (Iteration 1). In this configuration, the maximum gain achieved was 2.8 dB, as depicted in Figure 4 (Iteration 1). Moving on to iteration 2 of the design process, an elliptical slot was carefully introduced onto the previously circular patch. This transformation resulted in the patch taking on an arc-shaped configuration, guided by the principles described in Equation (1), as shown in Figure 1b. The introduction of this slot has a significant impact on the resonant frequency of the antenna, leading to the emergence of an additional resonating band close to the original resonant frequency, resulting in a dual-band response. Achieving optimal placement and orientation of the elliptical slot on the patch was crucial for attaining the desired wider bandwidth and increased gain. This optimization process involved fine-tuning the position of the elliptical slot on the radiating plane while closely monitoring its current distribution. As a result of these changes, the antenna exhibited a $|S_{11}|$ consistently below -10 dB over frequency ranges spanning 24 to 28.2 GHz (FBW of 13.12%) and 33.1 to 40 GHz (FBW of 21.56%), as demonstrated in Figure 4 (Iteration 2). In this configuration, the maximum gain achieved was 3.9 dB, as depicted in Figure 4 (Iteration 2).

$$r_A = \frac{F_0}{\left\{1 + \left(\frac{2H}{\pi K F_0} \left[\ln\left(\frac{\pi K F_0}{2H}\right) + 1.7726 \right]\right)\right\}^{\frac{1}{2}}} \quad (1)$$

where H is the height of the substrate, K dielectric constant and F_0 is the center frequency. The F_0 is given by Equation (2)

$$F_0 = \frac{8.791 \times 10^9}{f \sqrt{K}} \quad (2)$$

$$F_0 = \frac{8.791 \times 10^9}{32.5 \times 10^9 \sqrt{2.2}} = 0.18205$$

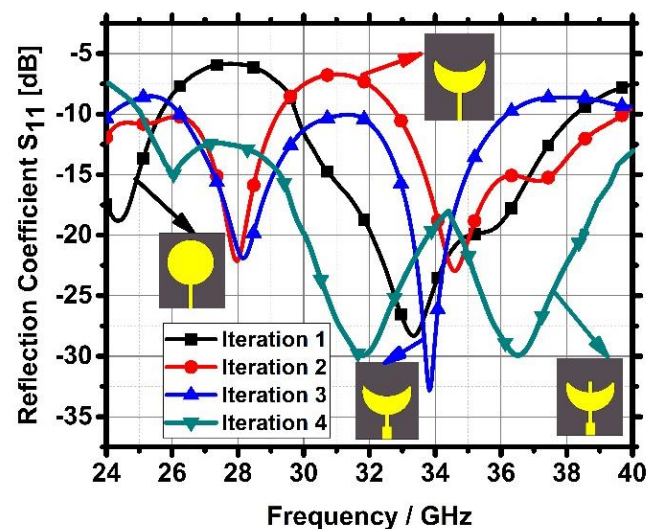


Figure 3. Reflection coefficient $|S_{11}|$ of all four iterations for a single antenna.

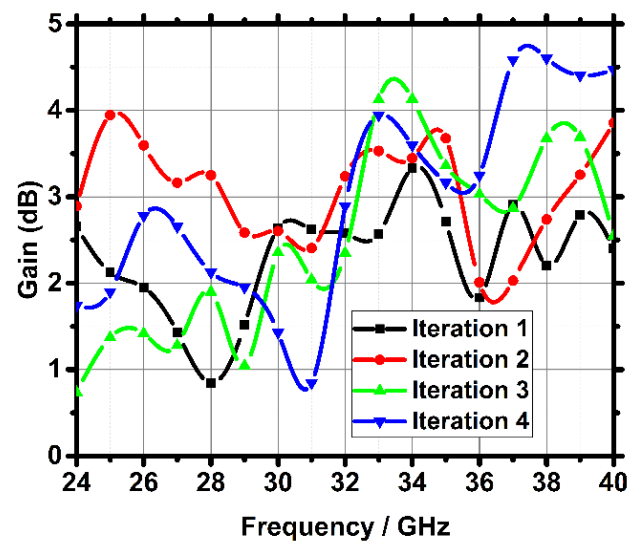


Figure 4. Comparison of gain for each iteration.

In the third iteration of the design, a QWT is introduced into the feed line, as illustrated in Figure 1c. The primary objective was to optimize impedance matching to enable efficient power transfer between the antennas. This resulted from the carefully choice of the QWT's length and characteristic impedance, which effectively changed the antenna's impedance to match the transmission line's characteristic impedance. This reduction in impedance mismatch losses significantly improved power transfer efficiency, ensuring effective energy transmission. In this specific configuration, the antenna demonstrated a wide operating bandwidth, ranging from 26.3 to 36.1 GHz (FWB of 31.41%). Two prominent resonances are observed at 28 GHz and 33.9 GHz, as indicated in Figure 3 (Iteration 3). Additionally, the maximum gain reached 4.4 dB, as shown in Figure 4 (Iteration 3). Moving on to Iteration 4, a rectangular stub was incorporated into the center of the arc-shaped patch, as depicted in Figure 1d. This design alteration aimed to achieve broad impedance-matching characteristics. Because of these improvements, the changed antenna consistently showed a reflection coefficient below -10 dB over a wider frequency range, from 25 to 40 GHz, with an FWB of 46.15%. Notable resonating frequencies are observed at 26 GHz, 31.8 GHz, and 36.5 GHz, as demonstrated in Figure 3 (Iteration 4).

In this particular configuration, the maximum gain is measured at 4.6 dB, as indicated in Figure 4 (Iteration 4).

Along with the current density meter, Figure 5 shows a full analysis of the arc-shaped patch antenna's current distribution at three different frequencies: 26 GHz, 31.8 GHz, and 36.5 GHz. This examination offers valuable insights into the antenna's behavior in response to electromagnetic fields at these specific frequencies. The visual representation of the current distribution is generated using a CST simulator. To convey the magnitude of the surface current of the antenna, a color gradient is employed, and the legend adjacent to each diagram corresponds to the magnitude levels. Specifically, blue indicates the minimum surface current while red signifies the maximum current. In Figure 5a, at 40 GHz, the QWT section with the transmission line exhibits a prominent red color, indicating a high current distribution, while the patch displays a lower current concentration. Conversely, Figure 5b shows an increased surface current distribution primarily focused on the patch. Figure 5c highlights that the maximum current distribution occurs at the patch, surpassing the observed current in Figure 5a,b. This observation indicates that the current intensity is at its peak at higher frequencies when compared with lower frequencies.

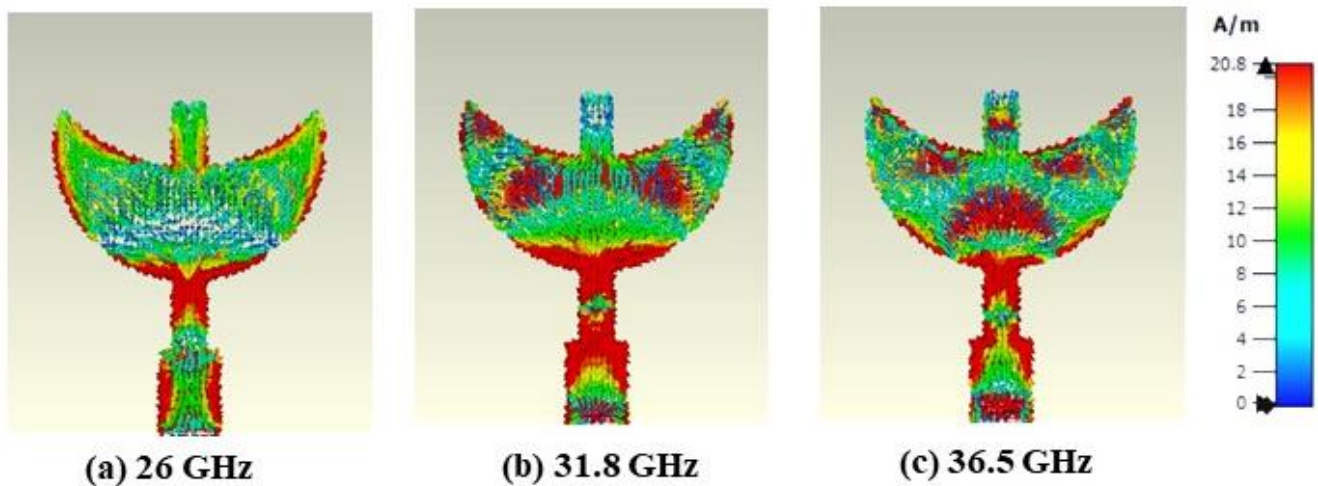


Figure 5. Surface current distribution.

3. Parametric Analysis of Single Antenna

One-patch antenna design is the focus of this section, which uses a detailed parametric analysis to examine the important factors that affect how it works. Figure 6a illustrates the variation of the radius (r) of the arc-shaped patch at different values. It is noteworthy that optimal performance in terms of the $||S_{11}||$ parameter is achieved when the radius is set at $r = 5.2$ mm. The antenna design under consideration incorporates a rectangular stub ($R1 \times R2$) positioned at the center of the arc-shaped patch, which plays a pivotal role in achieving a wide bandwidth within the desired frequency band. Figure 6b presents the variation of $R1$ at different values, revealing that $R1 = 3.3$ mm yields the most favorable outcomes in terms of bandwidth. Notably, as $R1$ values increase, there is a noticeable downward shift in the S_{11} graph towards lower frequencies. Furthermore, Figure 6b showcases the variation of $R2$ at different values, with $R2 = 1.8$ mm demonstrating the best results in terms of bandwidth. Conversely, as $R2$ values increase, the S_{11} graph exhibits poor impedance matching and shifts towards a higher magnitude. These findings provide valuable insights into optimizing the antenna design for enhanced performance.

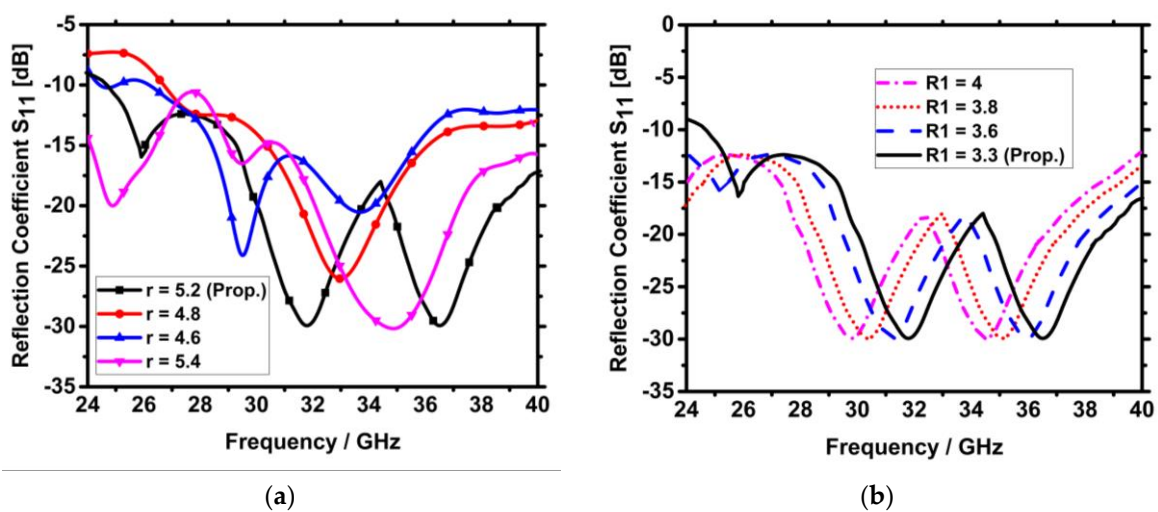
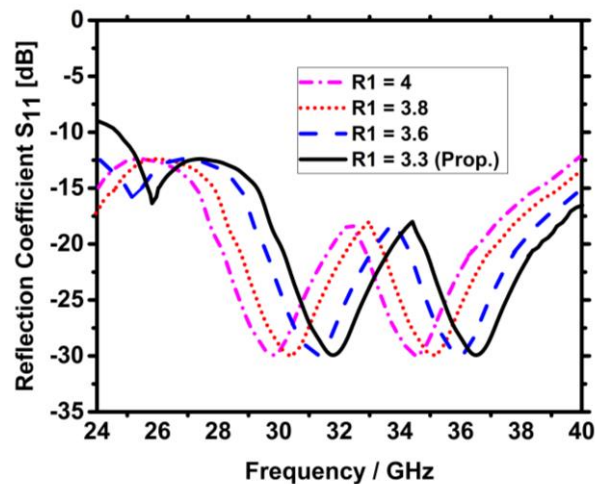


Figure 6. Cont.



(c)

Figure 6. (a) Variation of r (radius) of the arc-shaped patch at various values. (b) Variation of $R1$ (length of the rectangular stub) at various values. (c) Variation of $R2$ (width of the rectangular stub) at various values.

4. MIMO Antenna Configuration

In this section, we describe the transformation of a single antenna into a two-element orthogonally oriented MIMO antenna, as illustrated in Figure 7. This configuration serves to demonstrate the influence of element orientation on impedance matching and isolation between the antenna ports. The two antenna elements are placed on a common substrate with an edge-to-edge spacing of 3.5 mm. The mutual connection between the antenna elements has been observed in this configuration. To overcome the mutual coupling, we introduce a DGS with dimensions of $35 \times 35 \text{ mm}^2$ for both antenna elements. The modification of the ground surface involves removing two circular rings at the center and excluding eight metal strips with a rotational orientation. This altered ground structure acts as a barrier, limiting electromagnetic coupling between the two antennas.

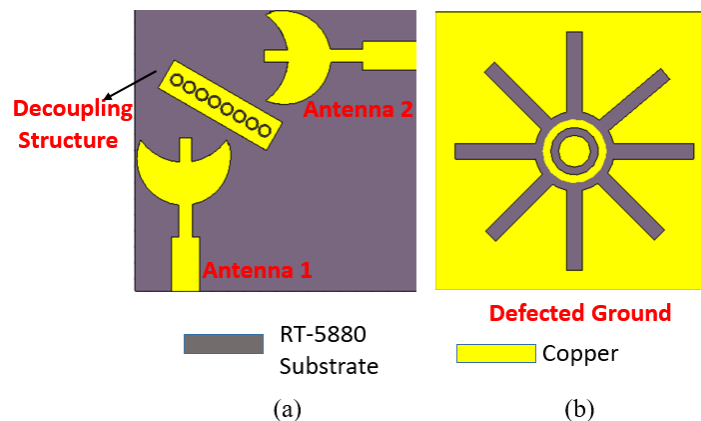


Figure 7. MIMO antenna configuration. (a) Top view and (b) bottom view (common DGS).

To enhance isolation further, we introduce a metal strip with a slotted ring-shaped structure between the antenna radiators, serving as an isolator. This slotted ring structure functions as a resonant element that impacts the currents on the antennas, thereby improving isolation. The MIMO antenna design boasts a compact size, straightforward structure, and cost-efficiency. We achieve wide-band operation by optimizing these parameters, covering the desired frequency range with three specific resonances at 28.5 GHz, 33 GHz, and 38.5 GHz.

Figure 8 represents symbols related to the dimensions of the antenna radiators, DGS, and decoupler, providing a visual representation of the antenna's physical layout. Parametric symbols and dimensions are presented in Table 3.

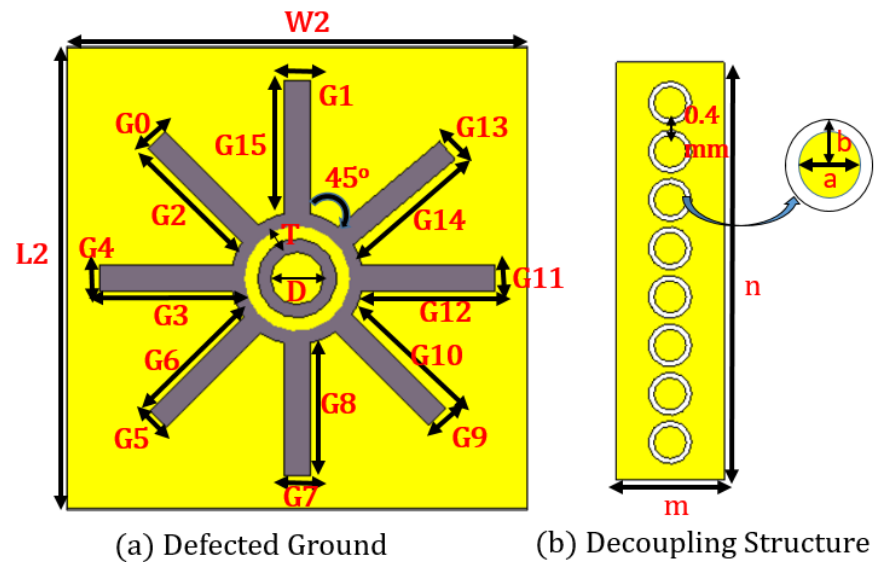


Figure 8. Symbols for each antenna element with dimensions.

5. Parametric Analysis of MIMO Antenna

To optimize the performance of the MIMO antenna, three different MIMO arrangements are proposed, and the DGS is the same for all versions, as shown in Figure 9. Each arrangement has a specific placement associated with it. In Version 1 of the MIMO antenna, if we incorporate a complete ground layer, there are observed mutual coupling issues, as illustrated in Figure 10. This acts as a reflective surface for the electromagnetic waves emitted by the antenna elements. These reflected waves can interfere with the radiation patterns of the antenna elements themselves, leading to mutual coupling. With the full ground layer employed, the achieved isolation is less than -16 dB. However, when the DGS is introduced, the isolation significantly improves to less than -23 dB.

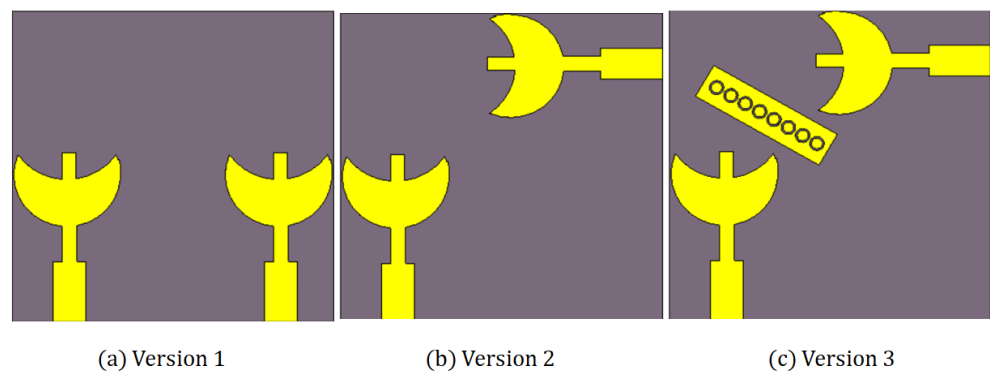


Figure 9. Parametric innovation of MIMO antenna with three antenna element orientations. (a) Linear alignment, (b) perpendicular configuration, and (c) perpendicular configuration with decoupler.

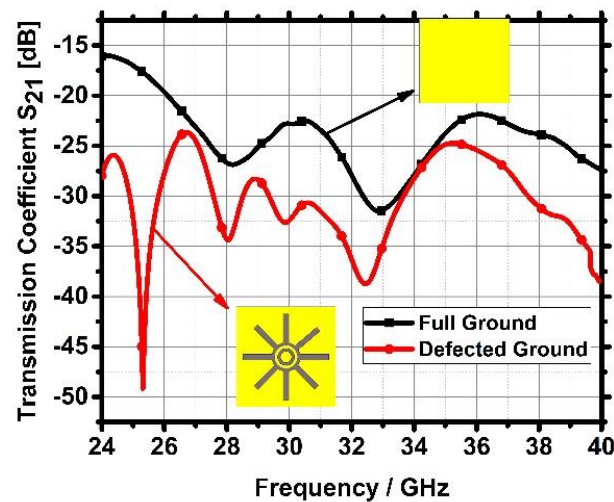


Figure 10. Transmission coefficient $|S_{21}|$ for version 1.

The initial antenna design, referred to as Version 1 with DGS (Figure 9a), incorporates two arc-shaped microstrip antennas arranged linearly and separated by a 4.3 mm gap. This arrangement is crucial for MIMO systems, where minimizing interference between antennas is paramount. This alteration is grounded in the principles of electromagnetic field behavior concerning distance. Specifically, the electromagnetic fields emitted by one antenna element decay more rapidly before reaching the other element, resulting in reduced mutual influence. As illustrated in Figure 9b, Version 2 takes things a step further by orienting the radiating components perpendicular to each other. This configuration further mitigates mutual coupling, consequently enhancing the antenna's performance. When antennas are oriented at right angles to each other, their radiation patterns are distinct, and their electromagnetic fields interfere less due to their orthogonal alignment. This diminishes the transfer of energy between the antennas. Moving to Version 3, a decoupler is introduced between the perpendicularly aligned radiators, as depicted in Figure 9c. This addition is aimed at optimizing and achieving peak performance for the MIMO antenna. The decoupling structure actively redirects electromagnetic fields away from each radiating element of the antenna. This is achieved through a meticulous design of the geometry, which generates resonance and field cancellation effects. These effects involve manipulating electromagnetic interference patterns and harnessing constructive and destructive interference from fields. By strategically placing the decoupler between the perpendicularly aligned radiators, the unwanted coupling is significantly minimized, resulting in improved isolation and overall antenna performance. Version 3 represents the proposed antenna design, featuring numerous enhancements that render it more efficient and effective for both transmitting and receiving signals.

Figure 11a–d shows the performance metrics of the antenna, including the reflection coefficient ($|S_{11}|$), transmission coefficient ($|S_{21}|$), gain and Z-parameters, for all three antenna versions. These metrics provide information about the behavior of antennas in various designs. In order to facilitate a comprehensive understanding of the optimization process, the comparative results of these three antenna versions (Version 1 to Version 3) are precisely summarized in Table 4. This tabular presentation of antenna design helps one to understand the delicate improvements and trade-offs achieved through various recapitulations.

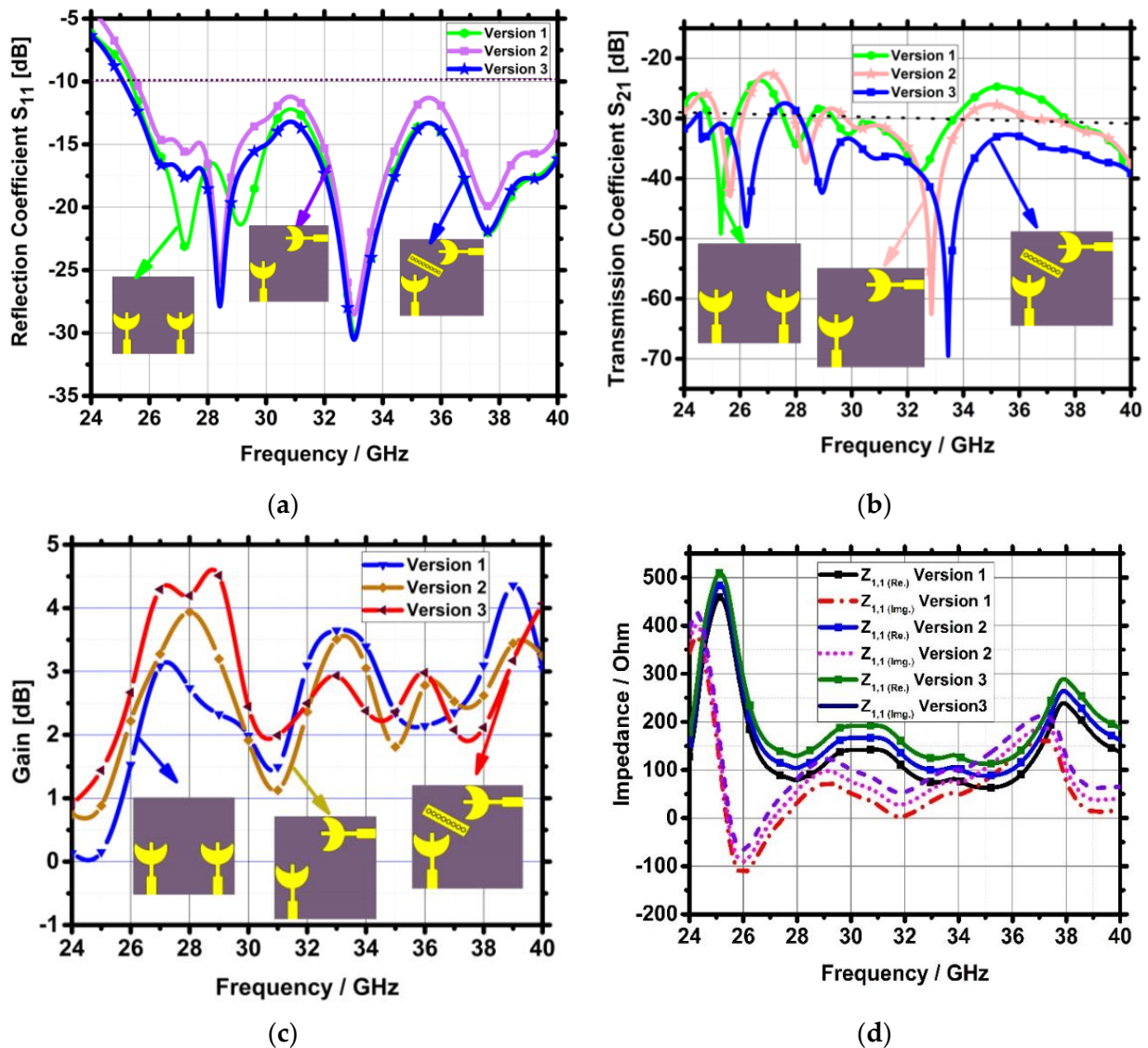
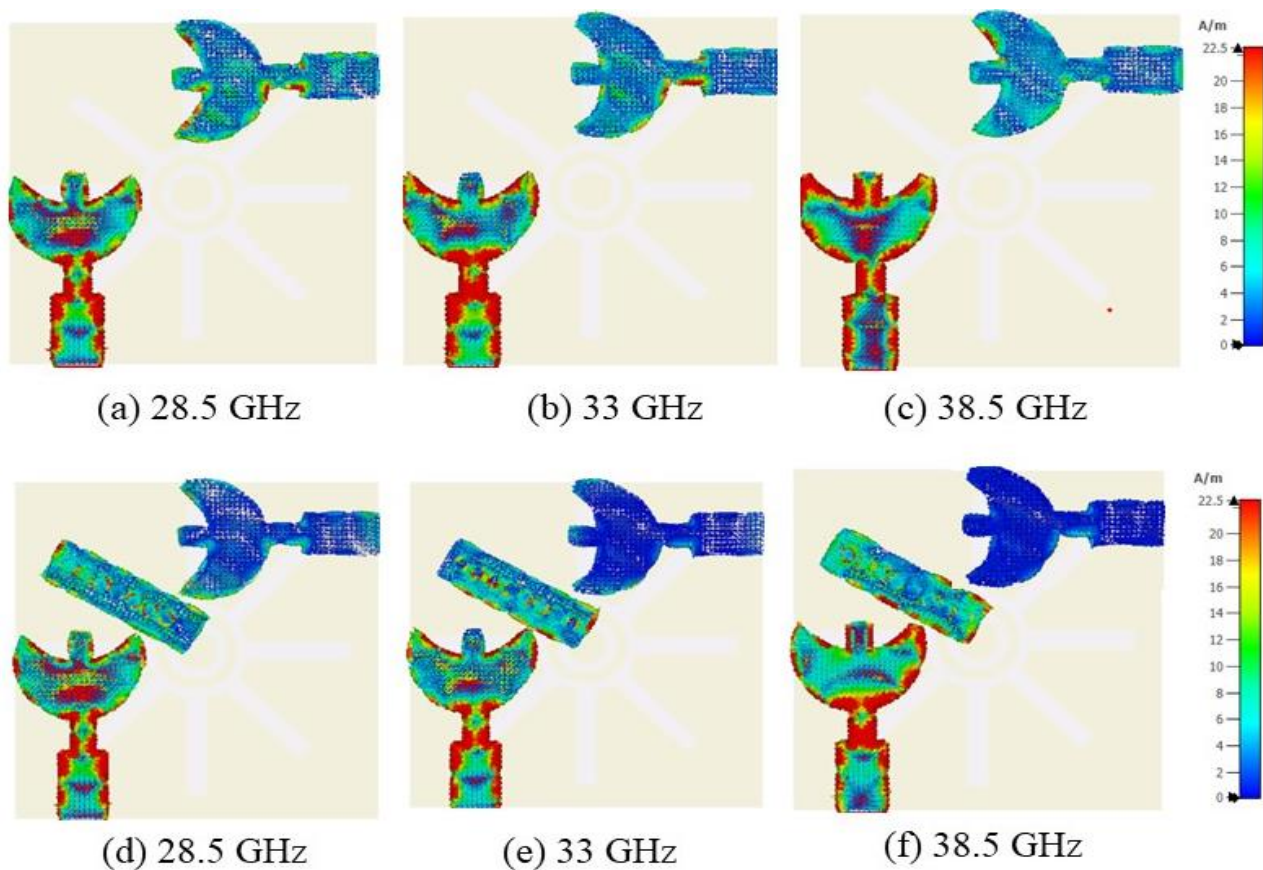


Figure 11. (a) Reflection coefficient $|S_{11}|$ for all three versions of antenna. (b) Transmission coefficient $|S_{21}|$ for all three versions of antenna. (c) Realized gain for all three versions of the antenna. (d) Z-parameters $|Z_{11}|$ for all three versions of the antenna.

The surface current distribution of the MIMO structure without a decoupler presented is shown in Figure 12a–c and with a decoupler is illustrated in Figure 12d–f, respectively, at 28.5 GHz, 33 GHz, and 38.5 GHz. In the simulation, one port is activated at a time, and the other is terminated with a 50Ω match load. Notably, when a specific port is energized, there is an observable current at the other ports. This indicates a need for reduced coupling between ports to enhance isolation. To achieve this, a distinctive decoupling structure is proposed to enhance isolation among the antenna elements. This design exploits the frequency dependence and interference pattern of the waveform to create a barrier against unwanted current transfer between closely spaced antennas. This concept takes advantage of the complex interplay of wave phenomena to achieve improved separation and performance within a MIMO antenna system. By situating a decoupler between the MIMO antenna elements, the energy transmission is theoretically entirely suppressed.

Table 4. Comparative results of these three antenna versions.

Versions	$ S_{11} $	$ S_{21} $	Gain	$ Z_{11} $
Version 1	< -10 dB from 25.3 to 40 GHz and 14.7 GHz bandwidth (PWB = 45.93%), minimum amplitude of -31.1 dB is obtained at 33 GHz.	> -23 dB	4.3 dB	Nearly 50Ω at 33 GHz
Version 2	< -10 dB from 25.25 to 40 GHz and 14.75 GHz (PWB = 46.09%), minimum amplitude of -31.1 dB at 33 GHz.	> -23 dB	3.5 dB	Nearly 50Ω at 33 GHz
Version 3	< -10 dB from 25 to 40 GHz, bandwidth of 15 GHz (PWB = 46.87%), minimum amplitude of -30.91 dB at 33 GHz.	> -28 dB	4.6 dB	Nearly 50Ω at 28.2 GHz a 33 GHz

**Figure 12.** Surface current distribution (a–c) without decoupler and (b–d) with decoupler.

6. Measurement Performance

The fabricated model of the proposed antenna is displayed in Figure 13a,b. The experimental results of the suggested antenna have been examined using an anechoic chamber and the VNA.

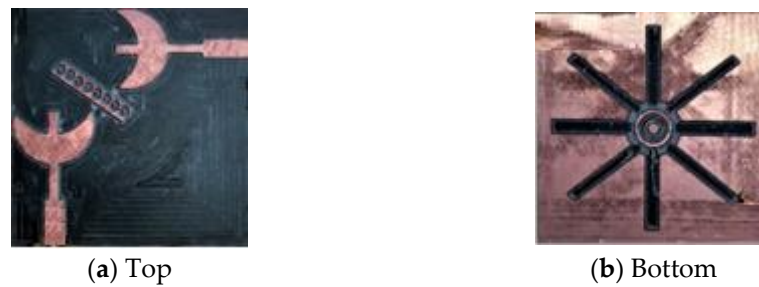


Figure 13. Fabricated model of proposed antenna. (a) Top surface and (b) bottom surface.

To validate the measurement outcome of $|S_{11}|$ of the proposed antenna under test (AUT), the use of VNA is presented in Figure 14. A comparison between simulated and measured outcomes was conducted to evaluate the accuracy of the simulation model and to determine the level of agreement between the theoretical predictions and experimental results.

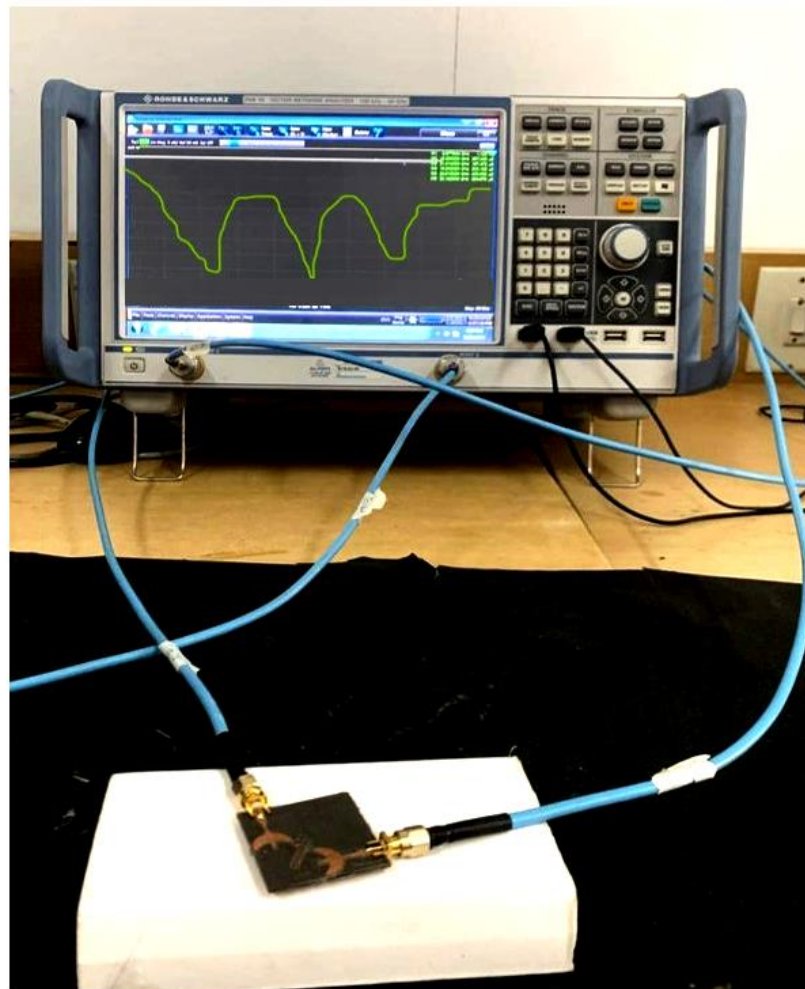


Figure 14. Antenna testing using VNA.

6.1. Scattering Parameters

Figure 15a,b demonstrates the comparison of simulated and measured scattering parameters in terms of $|S_{11}|$ and $|S_{21}|$, respectively, for the proposed antenna design. The measured $|S_{11}|$ for the antenna was found to be better than 10 dB for frequencies of 24.8–40 GHz and the bandwidth is 15.2 GHz (PBW = 47.5%) which closely matched with the simulated result. The simulated and measured mutual coupling, $|S_{21}|$, between the two input ports shows that the measured isolation was more than 27 dB (more than 30 dB

during 27.1–35.8 GHz) throughout the entire band. A mutual coupling level of less than 28 dB is adequate for MIMO applications throughout the entire frequency range.

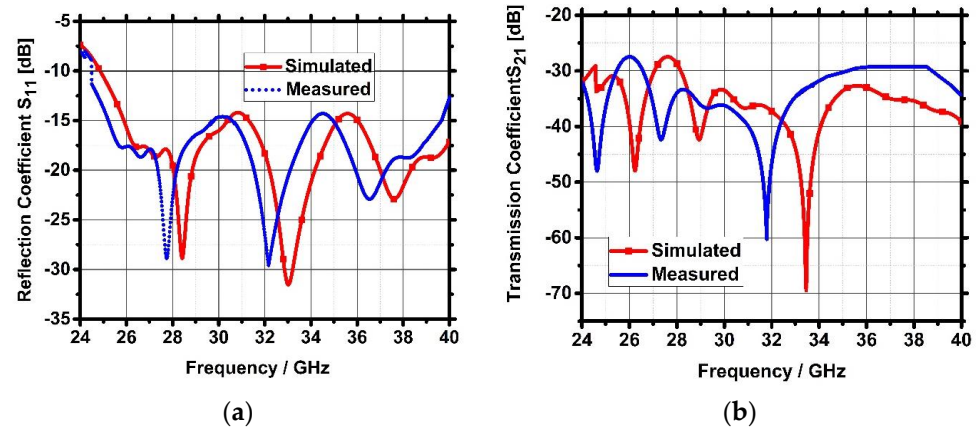


Figure 15. (a) $|S_{11}|$ of the proposed antenna. (b) $|S_{21}|$ of the proposed antenna.

The antenna demonstrates satisfactory performance for mm wave applications, but minor discrepancies in performance were noted due to connector interfacing and fabrication constraints.

6.2. Z-Parameter

The Z-matrix, also referred to as the impedance matrix, holds a pivotal role in characterizing antennas within electromagnetic theory. The Z-matrix comprises real and imaginary components, where the real part pertains to resistive aspects associated with power dissipation during electromagnetic wave radiation, while the imaginary part accounts for the phase disparity between voltage and current in the antenna's impedance. Figure 16 illustrates simulated and measured antenna impedance manifests in the Z-matrix. Notably, the diagonal elements of the Z-matrix, denoted as Z_{11} , signify the self-impedance of individual elements or points within the system. At resonance frequencies, the proposed antenna exhibits an impedance for its real part (Z_{11} real) that is approximately 50Ω , while the imaginary part (Z_{11} img.) is nearly negligible, approaching zero.

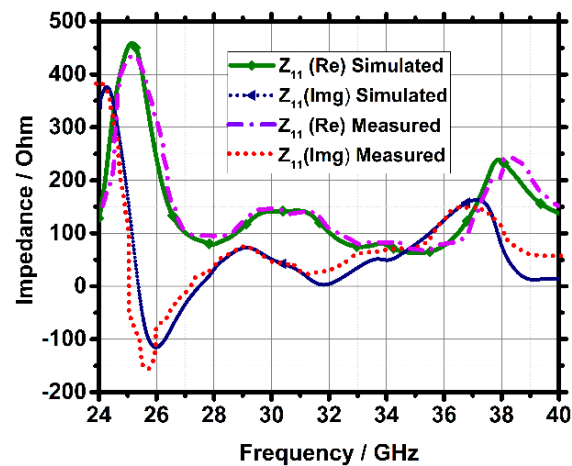


Figure 16. $|Z_{11}|$ of the proposed antenna.

6.3. Gain and Efficiency

The performance of the proposed MIMO antenna has been evaluated through simulations and measurements, and the obtained gain is presented in Figure 17a. The graph demonstrates that the antenna has achieved a remarkable gain of over 4.6 dB in the desired

band. These values are in good agreement with the experimental value of gain, which is 4.4 dB, indicating that the proposed antenna design is effective and reliable. Figure 17b illustrates a comparison between simulated and measured radiation and total efficiency. In the simulation, the radiation efficiency is 9.5 dB (95%), whereas in practical measurements, it is slightly lower, at 9.5 dB (95%). Similarly, the simulated total efficiency stands at 8.4 dB (84%), with a measured value of approximately 8.3 dB (83%). The achieved performance of the antenna is significant, as it meets the desired specifications and can potentially enable high-speed wireless communication systems in the mm wave frequency range.

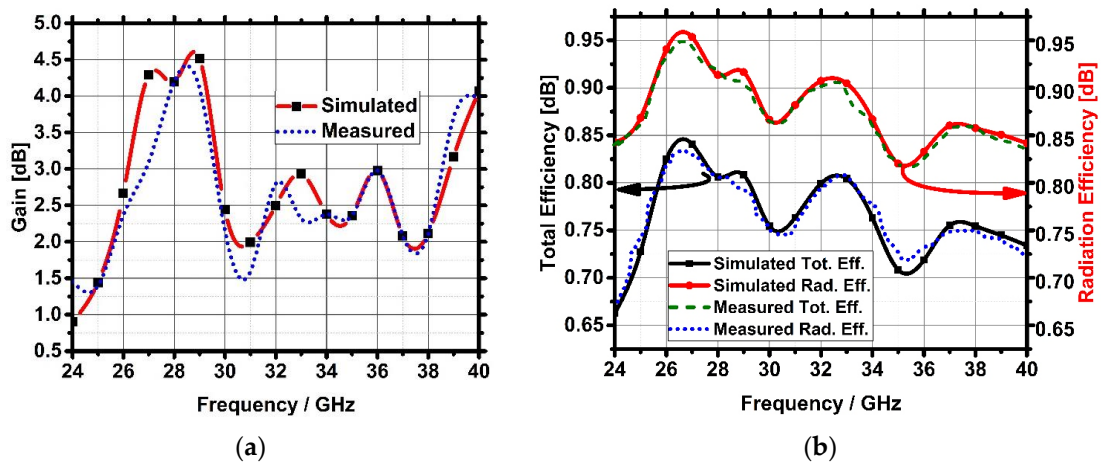


Figure 17. (a) Gain of the proposed antenna. (b) Efficiency of the proposed antenna.

6.4. Radiation Patterns

A two-dimensional (2D) radiation pattern represents the directional characteristics of an antenna or other electromagnetic radiation source in a two-dimensional plane. Figure 18a–d presents the 2D radiation patterns of the proposed antenna (for Port 1). Simulated radiation patterns are obtained using CST software and measured inside an anechoic chamber at frequencies of 28.5 GHz, 33 GHz, 36 GHz, and 38.5 GHz.

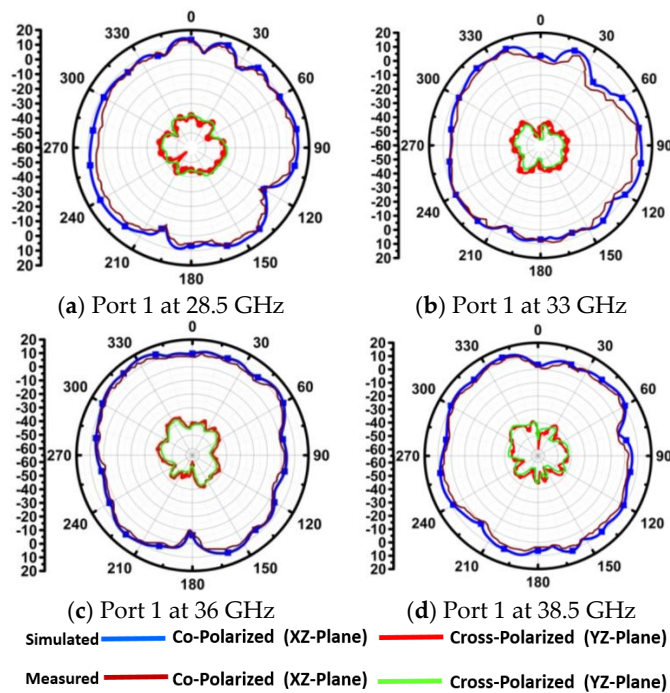


Figure 18. Two-dimensional radiation patterns of MIMO antenna xz-plane and yz-plane.

The measurement setup is displayed in Figure 19 for measuring the radiation patterns. When Port 1 is activated and Port 2 is terminated with a 50 Ω load, the radiation patterns of the antenna (port 1) are compared in terms of co-polarization (xz-plane) and cross-polarization (yz-plane) features, which are commonly used to evaluate 2D plots. The radiation patterns of the xz-plane and yz-plane are far from each other, showing low mutual coupling. The significance of these patterns lies in their ability to provide valuable insights into the antenna's performance characteristics, including its ability to transmit and receive signals in different polarizations.

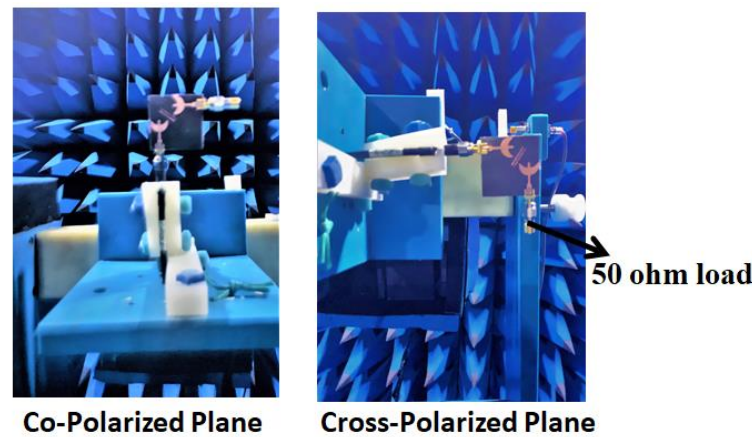


Figure 19. Measurement setup inside the anechoic chamber.

7. Diversity Characteristics

One way to measure the effectiveness of MIMO antennas is by evaluating their diversity, which can be assessed using two metrics: the ECC and DG.

7.1. Envelope Correlation Coefficient

ECC is an important parameter that determines the quality of the received signals and the overall system performance. A lower correlation coefficient between the antenna elements is desirable as it indicates greater diversity, which can lead to improved performance in MIMO systems. Theoretically, ECC can be estimated using Equation (3). The simulated and measured ECC is presented in Figure 20. The measured ECC is almost 0.0004, and the simulated value is 0.0016, within the acceptable threshold (i.e., less than 0.1) for the whole operating band for both ports.

$$ECC = \rho_e = \frac{|\iint F_1(\theta, \varphi) \cdot F_2(\theta, \varphi) |d\Omega|^2}{\iint |F_1(\theta, \varphi)|^2 d\Omega \iint |F_2(\theta, \varphi)|^2 d\Omega} \quad (3)$$

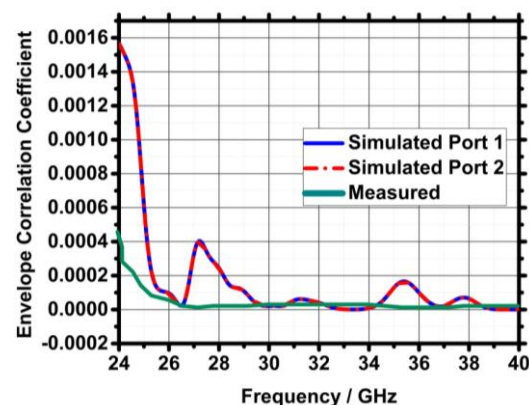


Figure 20. Envelope correlation coefficient of MIMO antenna.

7.2. Diversity Gain

DG refers to the improvement in signal quality achieved by utilizing multiple antennas at both the transmitter and receiver ends. It takes advantage of the spatial diversity for signal transmission and reception. Factors affecting DG include antenna count, spacing, and correlation. Increasing the number of antennas generally increases diversity gain, while larger spacing improves decorrelation and leads to higher gain. Figure 21 shows the simulated and measured diversity gain of the proposed antenna. It is observed from the measured outcomes that it exhibits a DG of almost 10 dB across its operating frequency band. Although the initial performance of both ports falls within the acceptable threshold, there is a slight reduction in the diversity gain to 9.992 dB in simulation outcomes, which is slightly below the ideal value of 10 dB. DG can also be determined using the ECC value in Equation (4).

$$DG = 10 \sqrt{1 - ECC^2} \quad (4)$$

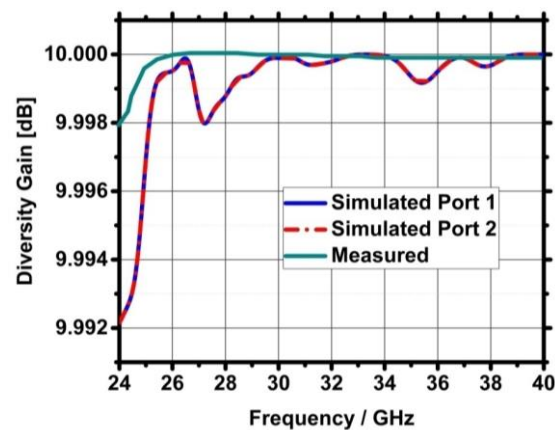


Figure 21. Diversity gain of MIMO antenna.

8. Conclusions

This work presents the evolutionary development of an antenna system, transitioning from a single antenna configuration to a MIMO setup. The fundamental antenna structure comprises two identical arc-shaped patches with DGS and decoupling mechanisms. Three different orientations were examined to improve the performance and dependability of the MIMO antenna. The goals were to reduce mutual coupling, improve impedance matching, and improve radiation characteristics. The resultant antenna, integrated with a decoupling structure, demonstrates exceptional parameters. These include an impressive 15 GHz bandwidth spanning from 25 to 40 GHz, outstanding isolation exceeding 28 dB, a maximum simulated gain of 4.6 dB, an ECC of 0.0016, and a DG of 9.992 dB. Experimental validation of the antenna affirms these remarkable attributes, with a measured bandwidth of 15.2 GHz, isolation surpassing 28 dB, and a commendable gain of 4.4 dB. Notably, the antenna exhibits remarkable diversity performance in practical testing, boasting an ECC of 0.004 and a DG of 10 dB. While minor discrepancies stemming from fabrication errors and measurement inconsistencies may exist, the simulation and measurement results exhibit close alignment. This aligns with the proposed antenna design's suitability for integration into wireless communication systems.

Author Contributions: Conceptualization, P.T., V.G. and M.K.; methodology, A.S. and I.E.; software, V.A. and V.G.; validation, P.T. and C.Z.; formal analysis, P.T. and A.S.; investigation, V.G. and C.Z.; resources, M.K. and J.R.; data curation, P.T.; writing—original draft preparation, P.T., V.G. and M.K.; writing—review and editing, V.A., C.Z. and I.E.; visualization, P.T. and M.K.; supervision, V.G., J.R. and I.E.; project administration, I.E. and J.R.; funding acquisition, I.E. and J.R. All authors have read and agreed to the published version of the manuscript.

Funding: This project has received funding from the European Union’s Horizon 2020 research and innovation program under grant agreement number H2020-MSCA-RISE-2018-EXPLOR-872897. This work is also funded by the FCT/MEC through national funds and when applicable co-financed by the ERDF, under the PT2020 Partnership Agreement under the UID/EEA/50008/2020 project.

Data Availability Statement: All the related data provided in the article.

Conflicts of Interest: The authors declare no conflict of interest.

References

1. Akpakwu, G.; Silva, B.; Hancke, G.; Mahfouz, A.A. A Survey on 5G Networks for the Internet of Things: Communication Technologies and Challenges. *IEEE Access* **2017**, *5*, 3619–3647. [[CrossRef](#)]
2. Zhang, J.A.; Cheng, P.; Weily, A.; Guo, Y. Towards 5th generation cellular mobile networks. *Aust. J. Telecommun. Digit. Econ.* **2014**, *2*, 34. [[CrossRef](#)]
3. Guevara, L.; Cheein, F.A. The role of 5G technologies: Challenges in smart cities and intelligent transportation systems. *Sustainability* **2020**, *12*, 6469. [[CrossRef](#)]
4. O’Connell, E.; Moore, D.; Newe, T. Challenges associated with implementing 5G in manufacturing. *Telecom* **2020**, *1*, 48–67. [[CrossRef](#)]
5. Zikria, Y.B.; Kim, S.W.; Afzal, M.K.; Wang, H.; Rehmani, M.H. 5G mobile services and scenarios: Challenges and solutions. *Sustainability* **2018**, *10*, 3626. [[CrossRef](#)]
6. Chávez-Santiago, R.; Szydełko, M.; Kliks, A. 5G: The Convergence of Wireless Communications. *Wirel. Pers. Commun.* **2015**, *83*, 1617–1642. [[CrossRef](#)]
7. Tiwari, P.; Gahlaut, V.; Kaushik, M.; Rani, P.; Shastri, A.; Singh, B. Advancing 5G Connectivity: A Comprehensive Review of MIMO Antennas for 5G Applications. *Int. J. Antennas Propag.* **2023**, *2023*, 5906721. [[CrossRef](#)]
8. Anguera, J.; Andújar, A.; Huynh, M.C.; Orlenius, C.; Picher, C.; Puente, C. Advances in antenna technology for wireless handheld devices. *Int. J. Antennas Propag.* **2013**, *2013*, 838364. [[CrossRef](#)]
9. Tiwari, P.; Kaushik, M.; Shastri, A.; Gahlaut, V. Design of a MIMO Rectangular Dielectric Resonator Antenna for 5G Millimeter-Wave Communications. In Proceedings of the 2023 IEEE Wireless Antenna and Microwave Symposium (WAMS), Ahmedabad, India, 7–10 June 2023; pp. 1–6.
10. Sunthari, P.M.; Veeramani, R. Multiband microstrip patch antenna for 5G wireless applications using MIMO techniques. In Proceedings of the 1st International Conference on Recent Advances in Aerospace Engineering (ICRAAE), Coimbatore, India, 3–4 March 2017; pp. 1–5.
11. Tiwari, P.; Gahlaut, V.; Kaushik, M.; Shastri, A.; Siddiqui, G.; Singh, B. A High-Frequency Planar-Configured Millimeter-Wave MIMO Antenna for Fifth-Generation NR Operations. In *International Journal of RF and Microwave Computer-Aided Engineering*; Wiley: Hoboken, NJ, USA, 2023.
12. Li, J.L.; Luo, M.H.; Liu, H. Design of a slot antenna for future 5G wireless communication systems. In Proceedings of the 2017 Progress Electromagnetics Research Symposium—Spring (PIERS), St Petersburg, Russia, 22–25 May 2017; pp. 739–741.
13. Al-Saedi, H.; Attari, J.A.; Wahab, W.M.A.; Mittra, R.; Safavi-Naeini, S. Single-feed dual-band aperture-coupled antenna for 5G applications. In Proceedings of the 2018 18th International Symposium on Antenna Technology and Applied Electromagnetics (ANTEM), Waterloo, ON, Canada, 19–22 August 2018; pp. 1–2.
14. Kammakattu, S.; Bora, P.; Mudaliar, M.; Dhanade, Y.; Madhav, B. Linear array Yagi-Uda 5G antenna for vehicular application. *Int. J. Eng. Technol.* **2017**, *7*, 513.
15. Huang, C.-Y.; Cheng, J.-C. Millimeter-Wave Leaky-Wave Antenna for 5G Mobile Phone. In Proceedings of the 2020 International Workshop on Electromagnetics: Applications and Student Innovation Competition (iWEM), Penghu, Taiwan, 26–28 August 2020; pp. 1–2.
16. González, R.M.; Márquez, R.T.R. Tri-Band Log-Periodic Microstrip Antenna Design (2.4, 5.5 and 3.6 GHz Bands) for Wireless Mobile Devices Application. In Proceedings of the International Congress of Telematics and Computing WITCOM, Puerto Vallarta, Mexico, 2–6 November 2020; pp. 18–29.
17. Andrews, J.G.; Buzzi, S.; Choi, W.; Hanly, S.V.; Lozano, A.; Soong, A.C.K.; Zhang, J.C. What will 5G be? *IEEE J. Sel. Areas Commun.* **2014**, *32*, 1065–1082. [[CrossRef](#)]
18. Shen, X.; Liu, Y.; Zhao, L.; Huang, G.; Shi, X.; Huang, Q. A miniaturized microstrip antenna array at 5G millimeter-wave band. *IEEE Antennas Wirel. Propag. Lett.* **2019**, *18*, 1671–1675. [[CrossRef](#)]
19. Jilani, S.F.; Alomainy, A. Millimeter-wave T-shaped MIMO antenna with defected ground structures for 5G cellular networks. *IET Microw. Antennas Propag.* **2018**, *12*, 672–677. [[CrossRef](#)]
20. Wei, K.; Zhang, Z.; Chen, W.; Feng, Z. A Novel Hybrid-Fed Patch Antenna with Pattern Diversity. *IEEE Antennas Wirel. Propag. Lett.* **2010**, *9*, 562–565. [[CrossRef](#)]
21. Kaiser, T.; Feng, Z.; Dimitrov, E. An overview of ultra-wideband systems with MIMO. *Proc. IEEE* **2009**, *97*, 285–312. [[CrossRef](#)]
22. Hong, W. Solving the 5G mobile antenna puzzle: Assessing future directions for the 5G mobile antenna paradigm shift. *IEEE Microw. Mag.* **2017**, *18*, 86–102. [[CrossRef](#)]
23. Munir, M.E.; Kiani, S.H.; Savci, H.S.; Marey, M.; Khan, J.; Mostafa, H.; Parchin, N.O. A Four Element mm-Wave MIMO Antenna System with Wide-Band and High Isolation Characteristics for 5G Applications. *Micromachines* **2023**, *14*, 776. [[CrossRef](#)] [[PubMed](#)]

24. Tiwari, P.; Kaushik, M.; Shastri, A.; Rai, J.; Gahlaut, V. Simulated Design and Analysis of Highly Isolated 5G Millimeter-Waves MIMO Antenna with Wideband Characteristic. In Proceedings of the International Conference on Microwave, Antenna and Communication (MAC) 2023, Allahabad, India, 24–26 March 2023.
25. Sokunbi, O.; Kishk, A. Millimeter-Wave MIMO Antenna With Decoupling Structures for Isolation Enhancement. In Proceedings of the 2023 17th European Conference on Antennas and Propagation (EuCAP), Florence, Italy, 26–31 March 2023; pp. 1–4.
26. Gaya, S.; Sokunbi, O.; Hamza, A.; Sheikh, S.I.M.; Attia, H. Multiple-input-multiple-output antenna with pattern reconfiguration and correlation reduction for WLAN applications. *Eng. Rep.* **2020**, *2*, e12272. [[CrossRef](#)]
27. Sang, L.; Hu, Z.; Wu, S.; Huang, W.; Tu, H.; Wang, W.; Chen, P.; Hong, W. A Dual-Band Planar Antenna Array with High-Frequency Ratio for Both Sub-6 Band and mm-Waveband. *IEEE Trans. Antennas Propag.* **2023**, *71*, 3856–3867. [[CrossRef](#)]
28. Tiwari, P.; Kaushik, M.; Shastri, A.; Gahlaut, V. Two Element Microstrip-Fed Slot Loaded Millimeter Wave MIMO Antenna. In Proceedings of the IEEE International Conference for Advancement in Technology (ICONAT), Goa, India, 24–26 January 2023; pp. 1–5.
29. Cuneray, K.; Akcam, N.; Okan, T.; Arican, G.O. 28/38 GHz dual-band MIMO antenna with wideband and high gain properties for 5G applications. *AEU-Int. J. Electron. Commun.* **2023**, *162*, 154553. [[CrossRef](#)]
30. Xie, M.; Wei, X.; Tang, Y.; Hu, D. A parasitic decoupling structure for dual-polarized patch antenna arrays. *IEEE Antennas Wirel. Propag. Lett.* **2023**, *22*, 1351–1355. [[CrossRef](#)]
31. Arya, V.; Garg, T.; Al-Khafaji, H.M.R. High Gain and Wide-Angle Continuous Beam Scanning SIW Leaky-Wave Antenna. *Electronics* **2023**, *12*, 370. [[CrossRef](#)]
32. Arya, V.; Garg, T.; Al-Khafaji, H.M.R. SIW Leaky Wave Antenna for THz Applications. *Electronics* **2023**, *12*, 1839. [[CrossRef](#)]
33. Arya, V.; Garg, T. Leaky Wave Antenna: Past and Present. In *Proceedings of Integrated Intelligence Enable Networks and Computing*; Singh Mer, K.K., Semwal, V.B., Bijalwan, V., Crespo, R.G., Eds.; Algorithms for Intelligent Systems; Springer: Berlin/Heidelberg, Germany, 2021.
34. Megahed, A.A.; Abdelhay, E.H.; Abdelazim, M.; Soliman, H.Y. 5G millimeter-wave wideband MIMO antenna arrays with high isolation. *EURASIP J. Wirel. Commun. Netw.* **2023**, *2023*, 61. [[CrossRef](#)]
35. Zhang, Y.M.; Yao, M.; Zhang, S. Wide-Band Decoupled Millimeter-Wave Antenna Array for Massive MIMO Systems. *IEEE Antennas Wirel. Propag. Lett.* **2023**, *37*, 1258–1273. [[CrossRef](#)]
36. Mistri, R.K.; Singh, A.K.; Mahto, S.K.; Sinha, R. Quad element millimetre-wave MIMO antenna for 5G communication. *J. Electromagn. Waves Appl.* **2023**, *7*, 1–23. [[CrossRef](#)]
37. Khabba, A.; Amadid, J.; Mohapatra, S.; El Ouadi, Z.; Ahmad, S.; Ibnyaich, S.; Zeroual, A. UWB dual-port self-decoupled o-shaped monopole MIMO antenna with small-size easily extendable design and high diversity performance for millimeter-wave 5G applications. *Appl. Phys. A* **2022**, *128*, 725. [[CrossRef](#)]
38. Al-Bawri, S.S.; Islam, M.T.; Shabbir, T.; Muhammad, G.; Islam, M.S.; Wong, H.Y. Hexagonal shaped near zero index (NZI) metamaterial-based MIMO antenna for millimeter-wave application. *IEEE Access* **2020**, *8*, 181003–181013. [[CrossRef](#)]
39. Sehrai, D.A.; Abdullah, M.; Altaf, A.; Kiani, S.H.; Muhammad, F.; Tufail, M.; Irfan, M.; Glowacz, A.; Rahman, S. A Novel High Gain Wideband MIMO Antenna for 5G MillimeterWave Applications. *Electronics* **2020**, *9*, 1031–1043. [[CrossRef](#)]
40. Khalid, M.; Naqvi, S.I.; Hussain, N.; Rahman, M.U.; Fawad Mirjavadi, S.S.; Khan, M.J.; Amin, Y. A 4-port MIMO antenna with defected ground structure for 5G millimeter wave applications. *Electronics* **2020**, *9*, 71–83. [[CrossRef](#)]
41. Aggarwal, R.; Roy, A.; Kumar, G. Comparative Analysis of Different Dielectric Substrate for the Design of Millimeter Wave Microstrip Patch Antenna. In *Computer Aided Constellation Management and Communication Satellites: Proceedings of the International Conference on Small Satellites, ICSS 2022 2023 Mar 1*; Springer Nature: Singapore; pp. 93–104.
42. Kumar, A.; Kumar, A.; Kumar, A. Defected Ground Structure Based High Gain, Wideband and High Diversity Performance Quad-Element MIMO Antenna Array for 5G Millimeter-Wave Communication. *Prog. Electromagn. Res. B* **2023**, *101*, 1–6. [[CrossRef](#)]
43. Rani, P.; Tiwari, P.; Singh, T.; Gahlaut, V. A Compact Ground Fed UWB Antenna with Single Band Notch Characteristics. In Proceedings of the 2021 2nd International Conference on Smart Electronics and Communication (ICOSEC), Trichy, India, 7–9 October 2021; pp. 435–440.
44. Ali, W.; Das, S.; Medkour, H.; Lakrit, S. Planar dual-band 27/39 GHz millimeter-wave MIMO antenna for 5G applications. *Microsyst. Technol.* **2021**, *27*, 283–292. [[CrossRef](#)]

Disclaimer/Publisher's Note: The statements, opinions and data contained in all publications are solely those of the individual author(s) and contributor(s) and not of MDPI and/or the editor(s). MDPI and/or the editor(s) disclaim responsibility for any injury to people or property resulting from any ideas, methods, instructions or products referred to in the content.